J. Fluid Mech. (2005), *vol.* 532, *pp.* 141–164.
doi:10.1017/S0022112005003964 Printed in the United Kingdom

Direct numerical simulation of turbulent flow in elliptical ducts

By NIKOLAY NIKITIN[1] AND ALEXANDER YAKHOT[2]

[1]Institute of Mechanics, Moscow State University, 1 Michurinsky prospect, 119899 Moscow, Russia

[2]The Pearlstone Centre for Aeronautical Engineering Studies, Department of Mechanical Engineering, Ben-Gurion University of the Negev, Beersheva 84105, Israel

(Received 6 June 2004 and in revised form 28 December 2004)

Direct numerical simulation (DNS) of fully developed turbulent flow in elliptical ducts is performed. The mean cross-stream secondary flows exhibited by two counter-rotating vortices which are symmetrical about the major ellipse's axis are examined. The mean flow characteristics and turbulence statistics are obtained. The variation of the statistical quantities such as the Reynolds stresses and turbulence intensities along the minor axis of the elliptical cross-section are found to be similar to plane channel data. The turbulent statistics along the major axis are found to be inhibited by the secondary flow transferring high-momentum fluid from the duct's centre towards the wall. The instantaneous velocity fields in the near-wall region reveal structures similar to the 'streaks' except in the vicinity of the major axis endpoints where significant reduction of the turbulent activity due to the wall transverse curvature effect is found.

1. Introduction

During the last decade, direct numerical simulation (DNS) has been recognized as a powerful and reliable tool for studying turbulent flows. Numerous studies showed that results obtained by DNS are in excellent agreement with experimental findings, if they are reliable (see Moin & Mahesh 1998). DNS-based studies are advantageous to experimental methods in that a practically unrestrained, far more detailed study of the flow-field structure can be achieved. Another, perhaps even more important advantage is that DNS allows exposure of new important physical mechanisms of turbulence production and self-sustainability. However, one major difficulty that arises with a numerical investigation of turbulent flow is the presence of a vast continuous range of excited scales of motion which must be correctly resolved by numerical simulation. DNS of turbulent wall-bounded flows requires order $Re^{21/8}$ storage and order $Re^{7/2}$ work to resolve dynamically significant velocity fluctuations at large Reynolds numbers. Even if computer power continues to increase at its present high rate, application of DNS to realistic flows of engineering importance will continue to be restricted by relatively moderate Reynolds numbers. Another principal restriction is that most DNS-based works have focused on simple-geometry flows. For wall-bounded turbulent flows, the majority of successful DNS-based simulations dealt with simple geometry cases such as a plane channel, a flat-plate boundary layer, a pipe and a straight square duct (see Kim, Moin, & Moser 1987; Spalart 1988; Gavrilakis 1992; Huser & Biringen 1993; Madabhushi & Vanka 1993; Eggels *et al.* 1994; Nikitin 1994, 1996, 1997). Discretization of Navier–Stokes equations in the vicinity of complex geometry boundaries is the most difficult problem for numerical simulating flow problems. The use of boundary-fitted, structured or non-structured grids solves this

problem, but implementing such grids leads to low-order numerical algorithms which involve high-cost computer time, are memory consuming, and cannot be efficiently used for DNS.

An alternative approach is based on the immersed-boundary (IB) method as introduced by Peskin (1972). IB methods were originally used to reduce the simulation of complex geometry flows to that defined on simple (rectangular) domains. This can be illustrated if we consider a flow of an incompressible fluid around an obstacle Ω (S is its boundary) placed onto a rectangular domain Π. The flow is governed by the Navier–Stokes and incompressibility equations with the no-slip boundary condition on S. The fundamental idea behind IB methods is to describe the flow problem, defined in $\Pi - \Omega$, by solving the governing equations inside an entire rectangular Π without an obstacle using simple rectangular (Cartesian or cylindrical) meshes, which, generally speaking, do not coincide with the boundary S. To impose the no-slip condition on an obstacle surface S (which becomes an internal surface for the rectangular domain wherein the problem is formulated), a source term $\boldsymbol{f}$ (an artificial body force) is added to the Navier–Stokes equations. The purpose of the forcing term is to impose the no-slip boundary condition on the $\boldsymbol{x}_S$-points which define the immersed boundary S.

IB-based approaches differ by the methods used to introduce an artificial force into the governing equations. References of different immersed-boundary methods can be found in Balaras (2004) and Moin (2002). For example, a 'direct forcing' approach was suggested by Mohd-Yusof (1997) for numerical schemes using spectral methods. Fadlun *et al.* (2000) and Kim, Kim & Choi (2001) developed the idea of 'direct forcing' for implementing finite-volume methods on a staggered grid. Kim *et al.* (2001) contributed two basic approaches for introducing direct forcing when using immersed-boundary methods. One was a new numerically stable interpolation procedure for evaluating the forcing term, and the other approach introduced a mass source/sink to enhance the solution's accuracy.

The main advantages of IB methods are that they are based on relatively simple numerical codes and highly effective algorithms, both of which result in considerable reduction of required computing resources. The main disadvantage, however, in using simple computational meshes is the difficulty in resolving local regions with steep (sharp, abrupt) variation of flow characteristics. These are especially pronounced for high-Reynolds number flows. In addition, in order to impose the boundary conditions, numerical algorithms require that the node velocity values should be interpolated onto the boundary points because the boundary S does not coincide with the gridpoints of a rectangular mesh. Finally, because of the time-stepping algorithms used in 'direct forcing' IB methods, the no-slip boundary condition is imposed with $O(\Delta t^2)$ accuracy. Therefore, implementation of IB methods to simulate turbulent flows requires careful monitoring to avoid possible contamination of numerical results arising from inaccurate boundary conditions.

Our present study is based on the direct forcing approach suggested by Kim *et al.* (2001). In this paper, we applied the IB method for DNS of fully developed turbulent flow in ducts with an elliptical cross-section. (The suggested numerical algorithm can be used for simulating flows in ducts of arbitrary cross-section.) An elliptical pipe is a slight modification of a classic pipe and the simplest type of non-circular duct. To the best of our knowledge, only Cain & Duffy (1971) have presented experimental data on turbulent flow in elliptical duct. As in other non-circular ducts, the flow is peculiar by developing secondary mean motions in the plane perpendicular to the streamwise flow direction known as secondary flows of the Prandtl second kind, and created

by generating the mean streamwise vorticity due to the anisotropy of the Reynolds stresses. Such motions are an intrinsic feature of turbulent flow in non-circular ducts and do not take place in a plane channel or a circular pipe. Despite the fact that the secondary velocity in non-circular ducts is only 1–3 % of the streamwise bulk velocity, secondary motions play a significant role by cross-stream transferring momentum, heat and mass (see Demuren & Rodi 1984). The development of turbulent closure models that can reliably predict turbulence-driven secondary flows in non-circular ducts is currently unfeasible owing to a lack of detailed experimental data. Reported DNS-based studies only relate to turbulent flow through straight ducts of square cross-section (see Gavrilakis 1992; Huser & Biringen 1993; Nikitin 1997). To the best of our knowledge, ours is the first study to perform a DNS of turbulent flow in elliptical ducts and to report the results of DNS calculations.

2. Numerical method: description and validation

We consider an incompressible fluid forced by pressure difference to move through an elliptical duct

$$G = \{(x, y, z): \quad x^2/a^2 + y^2/b^2 < 1, \ 0 \leqslant z \leqslant L_z\}. \tag{2.1}$$

Fully developed flow in a duct is governed by the Navier–Stokes equations

$$\frac{\partial \boldsymbol{u}}{\partial t} = -(\boldsymbol{u}\nabla)\boldsymbol{u} + \nu\nabla^2\boldsymbol{u} - \nabla p + \boldsymbol{k}\frac{\Delta p}{\rho L_z}, \tag{2.2}$$

subjected to the incompressibility constraint

$$\nabla \cdot \boldsymbol{u} = 0, \tag{2.3}$$

where $\boldsymbol{u} = (u_x, u_y, u_z)$ is the velocity field, p is the kinematic pressure, ν is the kinematic viscosity, and $\boldsymbol{k}$ is the unit vector in the z-direction. We imply the no-slip boundary condition at the wall and periodic boundary conditions in the streamwise z-direction. In (2.2), we split the pressure gradient into two terms, where, owing to the implied periodicity, the first (∇p) does not contribute to the overall pressure drop. In order to maintain a constant flow rate Q_0, the pressure drop is determined by the value of $\Delta p(t)$, which is obtained at each time instant from the constraint

$$\iint_{\Omega} u_z(x, y, z, t)\,\mathrm{d}x\,\mathrm{d}y = Q_0 = \text{const}. \tag{2.4}$$

In (2.4), Ω denotes the duct's cross-section, and the integral does not depend on z owing to incompressibility.

Numerical solution to the system of equations (2.2)–(2.3) was obtained by using the IB approach suggested by Kim *et al.* (2001). The only difference is that instead of using the time-advancement scheme of Rai & Moin (1991) we employed the algorithm suggested in Nikitin (1996). Both schemes exploit third-order accurate explicit Runge–Kutta methods for convective terms and second-order accurate implicit methods for viscous terms; thus, overall accuracy of both schemes is of second order in time. The advantage of the scheme we adapted is that it includes a built-in local accuracy estimation and time-step control algorithm. A variable time step is convenient, especially for simulations of flows with varying-in-time characteristic time scale, for example, for simulating a laminar–turbulent transition with randomly imposed initial perturbations. This process is usually accompanied by abrupt changes in the velocity field, which requires considerable reductions in the time-step size.

Following the IB approach, we solve the governing equations in a three-dimensional computational rectangular domain Π

$$\Pi = \{(x, y, z): \quad |x| \leqslant A,\ |y| \leqslant B,\ 0 \leqslant z \leqslant L_z,\ A > a,\ B > b\}, \tag{2.5}$$

which includes the elliptical (generally speaking, arbitrary) cross-section duct G, (2.1). We used the second-order accurate finite-difference discretization on a rectangular mesh incorporating the concept of staggered grids introduced by Harlow & Welsh (1965). Derivation of the finite-difference equations is similarly done as in Schumann (1975), but we also take into account the grid's non-uniformity in the x- and y-directions. The Poisson equation for the pressure is solved by fast direct methods using the fast Fourier transform in the z-direction and the cyclic reduction method in the (x, y)-plane (see Swarztrauber 1974).

The non-uniform grid in the cross-sectional plane was constructed using mapping of the uniform grid in computational space $-1 \leqslant \xi, \eta \leqslant 1$ by $x = Af(\xi),\ y = Bf(\eta)$. Here, the mapping function $f(\zeta) = \zeta[1+(1-\zeta^2)(7-3\zeta^2)/16]$ provides the gridpoints clustering near the boundaries $|x| = A,\ |y| = B$. In the axial z-direction the gridpoints were equally spaced.

The numerical procedure can be described as follows. Starting with some initial three-dimensional velocity field, the governing equations are integrated in time until a statistically steady state is reached. Then the mean flow and turbulence statistical quantities are obtained by further time-advancing and averaging both in time and along the homogeneous z-direction†. A result of this averaging procedure is that the mean fields depend on x and y.

In this paper, the presented results of the calculated velocities and turbulence intensities are normalized by the bulk velocity, U_b. The ellipse's major semi-axis, a, is the characteristic length; $l_\tau = \nu/u_\tau$ and $u_\tau = (\overline{\tau}_w/\rho)^{1/2}$ are the wall length and shear-velocity units, respectively‡. For the fully developed flow, the mean wall shear stress, $\overline{\tau}_w$, is balanced by the mean pressure drop, Δp, and defined from

$$\overline{\tau}_w = \Delta p \frac{D_h}{4L_z}, \qquad D_h = \frac{4\Omega}{P_w}, \tag{2.6}$$

where D_h is the hydraulic diameter, and Ω and P_w are the duct (ellipse) cross-section area and perimeter length, respectively.

2.1. *Circular pipe: computational domain, spatial and temporal resolution*

A cylindrical coordinate system is a natural choice for performing a simulation of a circular pipe flow. However, the application of the cylindrical coordinates causes some difficulty in implementing the numerical scheme. Besides the singularity at the centreline, the curvature of the cylindrical coordinates leads to small grid spacing close to the centreline, which may result in a strong restriction on the time step. Such peculiarities that arise when employing a cylindrical coordinate system for DNS of turbulent flows have been addressed in Eggels *et al.* (1994), Fukagata & Kasagi (2002), Morinishi, Vasilyev & Ogi (2004) and Verzicco & Orlandi (1996). The IB method used in this study does not encounter these difficulties. To validate the method, DNS of turbulent flow through a circular pipe was carried out. This

† In this paper, $\langle\rangle$ denotes averaging in time and over the streamwise direction. For convenience, an upper case letter Ξ is used for $\Xi \equiv \langle\xi\rangle$. A quantity ξ' means an instantaneous fluctuation of ξ, i.e. $\xi = \langle\xi\rangle + \xi'$.

‡ For ξ^+, the subscript $^+$ denotes that a quantity ξ is normalized by the wall units.

Case	CP1	CP2	CP3
$Re_m = U_b D/\nu$	4000	4000	6000
$N_x \times N_y \times N_z$	$64 \times 64 \times 64$	$120 \times 120 \times 128$	$120 \times 120 \times 128$
$Re_\tau = u_\tau a/\nu$	142	141	204
L_z/a	6.0	6.0	6.0
L_z^+	851	846	1227
$h^+_{x,y,min}$	2.3	1.2	1.7
$h^+_{x,y,max}$	6.6	3.4	5.0
h_x^+	4.6	2.4	3.5
h_y^+	4.6	2.4	3.5
h_z^+	13.3	6.6	9.6
Δs^+	6.5	3.4	4.9
Δ^+	6.5	3.4	4.9
$d^+_{1,min}$	0.0	0.0	0.0
$d^+_{1,max}$	2.3	1.5	2.2
$d^+_{1,mean}$	1.2	0.7	1.0
Δt^+	0.5	0.25	0.35
CFL	0.7	0.7	0.7
$T_{av} u_\tau/a$	570	30	40
C_f	0.0101	0.00994	0.00929
$\Delta(C_f)$	1.2 %	−0.03 %	3.4 %
U_c/U_b	1.32	1.33	1.30
U_c^+	18.66	18.81	19.10

TABLE 1. Circular pipe runs.

flow has been thoroughly studied and has been documented both experimentally and numerically. Comprehensive analysis of the DNS-based results are in excellent agreement with experimental findings (see Eggels *et al.* 1994; Nikitin 1994, 1996). This means that a circular pipe case can be used as a benchmark test for the immersed-boundary method. We have performed three test simulations of turbulent flow in a circular pipe ($a = b$, $D = 2a$). The mean flow properties and computational grid data are summarized in table 1. The computational domain cross-section, (2.5), is a square, $A = B$; the length of its side has been specified to exceed the diameter of the pipe by 4 grid cells. The length of the computational domain, L_z, is of 6 pipe radii, which is less than that used in Eggels *et al.* (1994) and Kim *et al.* (1987) (10 and 4π, respectively). As has been shown in Nikitin (1994, 1996), $L_z \approx 6a$ is sufficient for satisfactorily predicting the main turbulence statistics properties. In table 1, the smallest and largest gridspacings in the x- and y-directions are denoted by $h_{x,y,min}$ and $h_{x,y,max}$, respectively (because of the symmetry, the gridpoints were similarly distributed in the x- and y-directions). The mean gridspacings of the cells located inside the pipe are h_x and h_y; the gridspacing in the z-direction, h_z, is uniform.

For DNS of wall-bounded flows, the spatial discretization at the given Reynolds number should be chosen so that all dynamically relevant length scales in the near-wall region are properly resolved. It is convenient to use the viscous length scale ν/u_τ as the measure of the smallest turbulence scale. The distance to the wall of the first gridpoint (d_1), where the axial velocity is computed, should be of the order of ν/u_τ or less. From table 1, only the case CP2 somewhat satisfies this requirement. We note that the pipe's boundary intersects the computational cells in an irregular

manner. Moreover, most of the grid points nearest to the boundary surface, where the axial velocity is calculated, are located at a distance less than the near-wall cell size. The spanwise (circumferential) resolution in the near-wall region can be estimated as $\Delta s \approx \sqrt{h_x^2 + h_y^2}$. For all cases given in table 1, the resolution was sufficient to resolve the near-wall streaks with the mean spanwise spacing of $\lambda^+ \simeq 80$–120. It is believed that the mean grid width $\Delta^+ = (h_x^+ h_y^+ h_z^+)^{1/3}$ satisfies the constraint $\Delta^+ \leqslant \pi\eta^+$, where η^+ is the Kolmogorov length scale (see Eggels *et al.* 1994). With $\eta^+ \approx 1.6$, the criterion $\Delta^+ \leqslant 5.0$ is satisfied for cases CP2 and CP3.

The time steps Δt in table 1 correspond to a fully developed regime. The initial velocity field with imposed randomly chosen perturbations undergoes transition to turbulence through non-physical states. This process might be accompanied by abrupt changes of the velocity field, which requires reducing the time step. This was done using an effective time-step control procedure developed in Nikitin (1996). As was noted in § 1 the 'direct forcing' IB method developed by Kim *et al.* (2001) and employed in this paper introduces an error of $O(\Delta t^2)$ in the no-slip boundary condition. To estimate this error, the maximum of the velocity components at the boundary points have to be monitored in time. The criterion for the time step Δt in our circular pipe test calculations (as well as in simulations of elliptical duct flows considered below) was to maintain the maximum error in the no-slip condition at a level of 2–$3 \times 10^{-3} U_b$. It should be emphasized that the error L_2-norm is about one order of magnitude less than the maximum value. Besides the requirement to minimize the error in the no-slip condition, the resolution in time should be sufficiently small to resolve all scales of motion. For the so-called 'minimal flow unit' of Jiménez & Moin (1991) – the computational domain with minimum sizes in the streamwise and spanwise directions to sustain channel flow turbulence – Choi & Moin (1994) demonstrated that the computational time step should be perceptibly less than the Kolmogorov time scale in the viscous sublayer, $\tau^+ \equiv (u_\tau^4/\varepsilon\nu)^{1/2} \simeq 2.4$, where ε is the dissipation rate. Their computations indicated that the turbulence statistics obtained with the non-dimensional time step $\Delta t^+ = 0.4$ are sufficiently close to those predicted with $\Delta t^+ = 0.2$. DNS of turbulent flow in a full channel showed that the estimation $\Delta t^+ \leqslant 0.2$ is apparently too conservative. On the other hand, simulations with $\Delta t^+ \sim 1.0$ predicted very good turbulence statistics (see Nikitin 1994, 1996, 1997). For DNS of a circular pipe flow, Eggels *et al.* (1994) used $\Delta t^+ = 0.072$, which is much smaller than the Kolmogorov time scale. Akselvoll & Moin (1996) used a domain decomposition method for temporal integration of the Navier–Stokes equations written in cylindrical coordinates. Their method yielded the maximum time step $\Delta t^+ = 0.18$, which is a factor 2.5 higher than that employed in Eggels *et al.* (1994). The time steps used in this study are presented in table 1. As is clear from table 1 (and from the simulations of turbulent flows in elliptical ducts discussed in the next section, table 2), the numerical scheme used in this study allows the time steps $\Delta t^+ = 0.16$–0.5. These computational time steps correspond to reasonable CFL numbers, $\mathrm{CFL} = \Delta t \max\{u_x/h_x, u_y/h_y, u_z/h_z\}$.

2.2. *Circular pipe: mean flow and turbulence statistics properties*

Statistically steady-state data for DNS of turbulent flows in a pipe using a cylindrical coordinate system are usually generated by spatial averaging over the homogenous streamwise and circumferential directions and by averaging in time. The time-averaging interval, normally used to reach the time-independent turbulence statistics by averaging over two homogeneous direction, is $T_{av} = 5$–$10 a/u_\tau$, where a/u_τ is the time scale usually referred to as the 'turnover time'. For the IB method, which is based

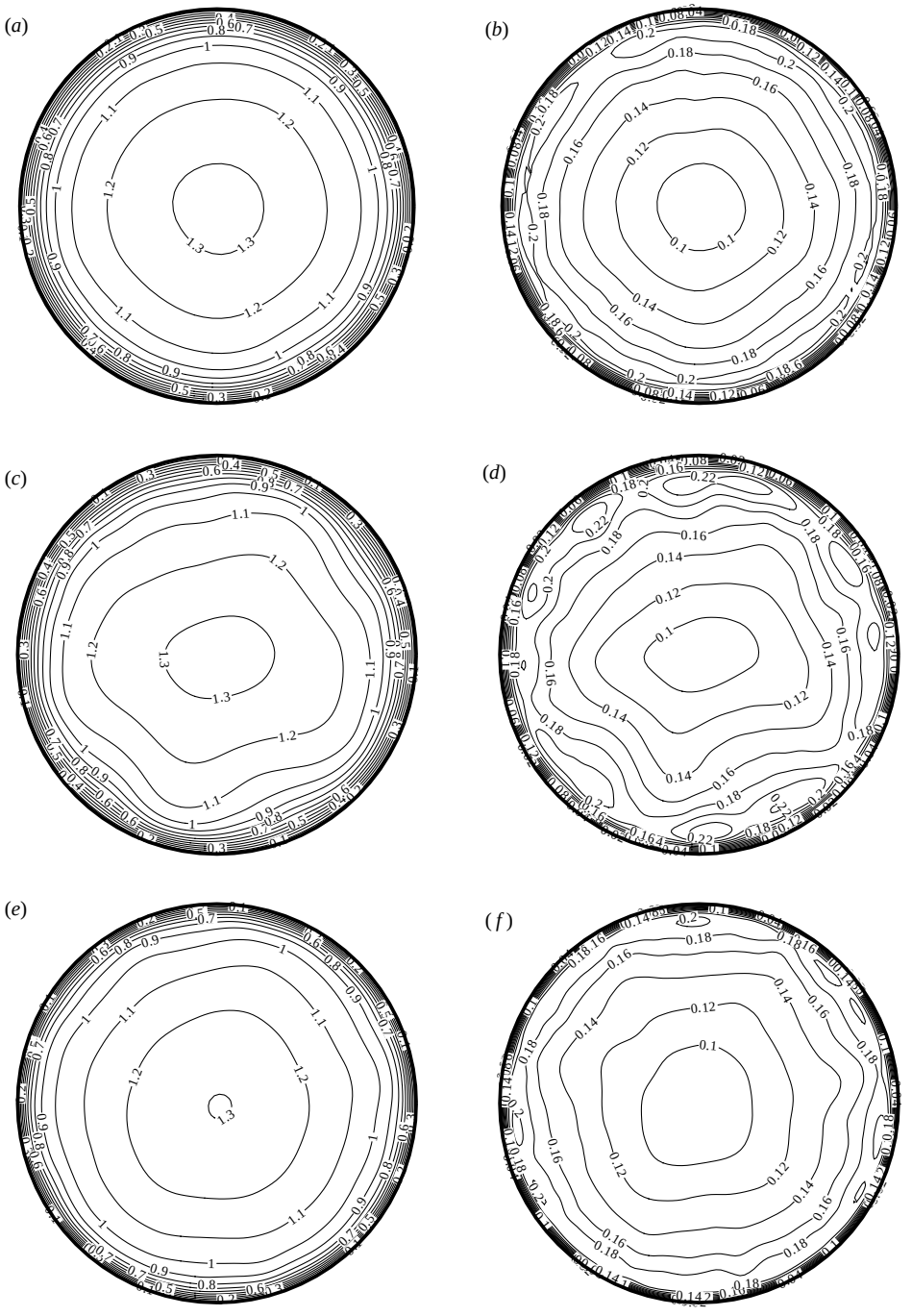

FIGURE 1. Contours of (a, c, e) U_z and (b, d, f) $|\boldsymbol{u}'|_{rms}$; (a, b)CP1, (c, d)CP2, (e, f)CP3.

on a Cartesian coordinate system, averaging over one homogenous streamwise direction is insufficient, for which T_{av} must be considerably increased. In figure 1, we show the contours of the averaged streamwise velocity U_z normalized by the bulk velocity U_b and the root-mean-square of the velocity total fluctuations $|\boldsymbol{u}'|_{rms} = \langle u_x'^2 + u_y'^2 + u_z'^2 \rangle^{1/2}$.

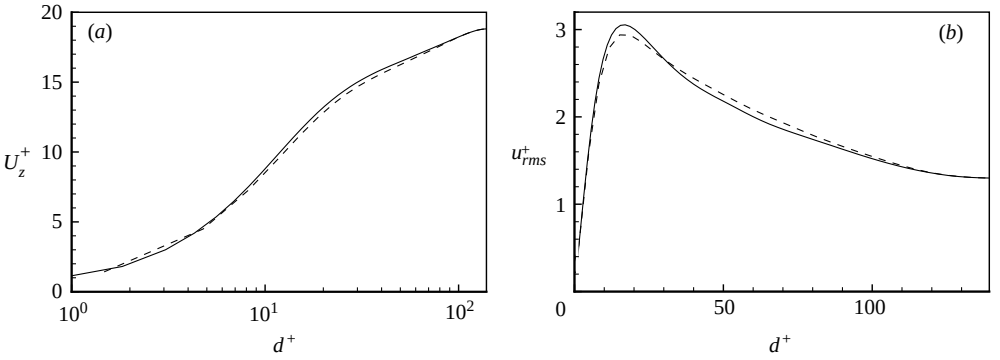

FIGURE 2. Radial distribution of (*a*) U_z and (*b*) $|\boldsymbol{u}'|_{rms}$ averaged over four radii; —, $\theta = 0$, $\pi/2$, π, $3\pi/2$; – – –, $\theta = \pi/4$, $3\pi/4$, $5\pi/4$, $7\pi/4$.

For the cases CP2 and CP3, the insufficiency of the time-averaging intervals is exhibited by the azimuthal asymmetry. As seen from table 1, the time-averaging interval $T_{av} = 570a/u_\tau$, employed for case C1, was larger than that of case CP2 by a factor of about 20. Thus, it can be inferred that for a relatively short computational domain $L_z/a = 6$ (as used for our circular pipe simulations), the time-averaging interval should be several hundreds of a turn-over time measured in a/u_τ units.

In figure 2, the radial distributions of U_z and $|\boldsymbol{u}'|_{rms}$ averaged over two sets of four radii ($\{\theta_{\pi/2}\} = \{0, \pi/2, \pi, 3\pi/2\}$ and $\{\theta_{\pi/4}\} = \{\pi/4, 3\pi/4, 5\pi/4, 7\pi/4\}$) are shown for case CP2 which was performed with the smallest time-averaging interval. It should be especially noted that this additional radius-averaging is effectively equivalent to the increasing T_{av} by a factor of 4. The four radii of the $\{\theta_{\pi/2}\}$-set are parallel to the co-ordinate lines, while those of the $\{\theta_{\pi/4}\}$-set intersect them at angle $\pi/4$. Despite the lack of axial symmetry (figures 1*c*, *d*, CP2) and different orientation of the radii with respect to the Cartesian coordinate lines, the data in figure 2 show no significant angular anisotropy. A similar radius-averaging procedure applied to cases CP1 and CP3 resulted in practically identical distributions along the radii $\{\theta_{\pi/4}\}$ and $\{\theta_{\pi/4}\}$.

In table 1, C_f is the friction coefficient computed from the DNS data,

$$C_f = 2\overline{\tau}_w/\rho U_b^2, \tag{2.7}$$

where $\overline{\tau}_w$ is defined in (2.6) and $\Delta(C_f)$ is the relative deviation of the calculated C_f from that of the Blasius' law, namely

$$C_f = 0.0791\, Re_m^{-0.25}. \tag{2.8}$$

The present results are in good agreement with Blasius' law for $Re_m = 6000$, and for $Re_m = 4000$ the agreement is even better.

Figure 3 shows the mean streamwise velocity $U_z(d)$ normalized by the wall shear velocity as a function of the distance to the wall d. $U_z(d)$ is computed by averaging $\langle u_z \rangle$ in the θ-direction ($\theta = \tan^{-1}(y/x)$, $d = a - \sqrt{x^2 + y^2}$)

$$U_z(d) = \int_0^{2\pi} \langle u_z \rangle \, \mathrm{d}\theta. \tag{2.9}$$

To compute the integral in (2.9), the velocity value $\langle u_z \rangle$ at given r and θ is obtained using a bilinear interpolation from the surrounding gridpoints. In figure 3, the velocity profiles obtained in Nikitin (1994, 1996) for the same Reynolds numbers by a spectral/finite-difference method in cylindrical coordinates are shown for comparison.

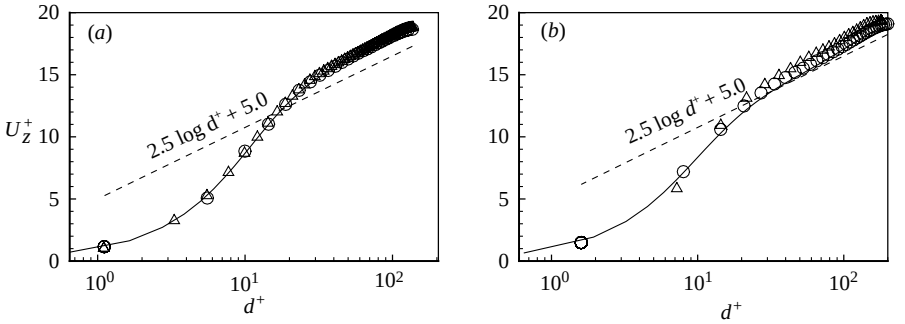

FIGURE 3. Streamwise mean velocity logarithmic profile. (*a*) $Re_m = 4000$; ○, CP1; △, CP2; —, Nikitin (1994, 1996). (*b*) $Re_m = 6000$; ○, CP3; —, Nikitin (1996), △, Eggels *et al.* (1994).

In figure 3(*b*), the velocity for a somewhat lower Reynolds number ($Re_m = 5300$) taken from Eggels *et al.* (1994) is also shown. Figures 3(*a*) and 3(*b*) show a close agreement between the results obtained by different numerical methods, which confirms the successful grid-refinement test carried out for $Re_m = 4000$.

For the range of Reynolds numbers considered in this paper, the mean velocity profile in a circular pipe differs from that in a channel (see Kim *et al.* 1987; Nikitin 1996; Moser, Kim & Mansour 1999), where $U_z^+ = \kappa^{-1} \log d^+ + B$ with the universal constants commonly referred to as $\kappa = 0.4$ and $B = 5.0$. However, a discussion of this issue is beyond the scope of this paper. Here, we are interested only in demonstrating that the DNS results obtained in the cylindrical and Cartesian coordinates agree remarkably well.

Our calculations confirm that the mean properties of turbulent flow in a pipe are in good agreement with those in a square duct as reported by Eggels *et al.* (1994). In particular, the values of U_c/U_b (U_c is the centreline velocity) given in table 1 are very close to those obtained in a square duct ($U_c/U_b = 1.33$ for $Re_m = 4410$ in Gavrilakis (1992) and $U_c/U_b = 1.32$ for $Re_m = 4000$ and 7500 in Nikitin (1997)). In a plane channel, this ratio is significantly smaller, $U_c/U_b = 1.16$ and 1.166 for $Re_m = 5600$ in Kim *et al.* (1987) and Nikitin (1996), respectively.

For $Re_m = 4000$, the r.m.s. of the turbulence intensities in the axial ($u_{z,rms}$), radial ($u_{r,rms}$), and azimuthal ($u_{\theta,rms}$) directions and the Reynolds shear stress $\langle u'_z u'_r \rangle$ are shown in figures 4(*a*) to (*d*). The velocity intensities in cylindrical coordinates are computed from: $u'_r = u'_x \cos\theta + u'_y \sin\theta$, $u'_\theta = -u'_x \sin\theta + u'_y \cos\theta$, $\tan\theta = y/x$; the results are averaged in the angular θ-direction. The results agree well with those obtained in Nikitin (1994, 1996) using cylindrical coordinates. From figure 5, it can be seen that there is good agreement between the turbulence statistics obtained for $Re_m = 6000$ and those in Eggels *et al.* (1994) and Nikitin (1996), especially if we take into account that Eggels *et al.* (1994) used a smaller Reynolds number for the simulations.

3. Elliptical ducts: DNS results

In this paper, geometrical and computational domain parameters are scaled on the length of the ellipse's major semi-axis a. Two elliptical ducts were considered: $b/a = 0.67$ (hereinafter referred to as 'wide') and $b/a = 0.5$ (hereinafter referred to as 'narrow'). The simulations were carried out for $Re_{D_h} = 6000$, where Re_{D_h} is the Reynolds number based on the bulk velocity U_b and the hydraulic diameter D_h defined in (2.6). Simulation parameters are summarized in table 2. The wall unit scales are

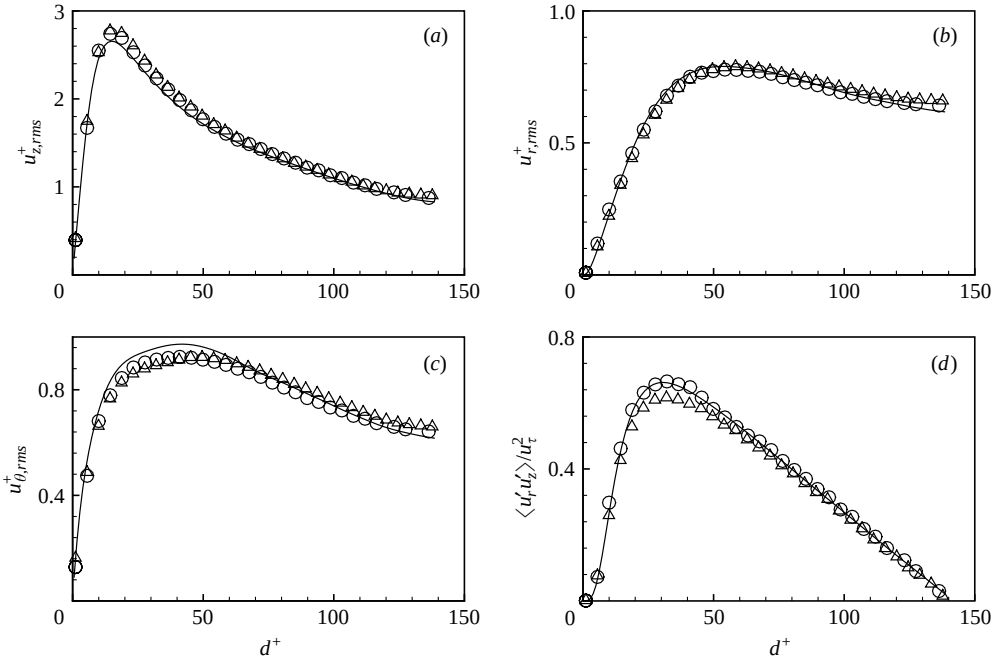

FIGURE 4. Symbols as for figure 3(*a*).

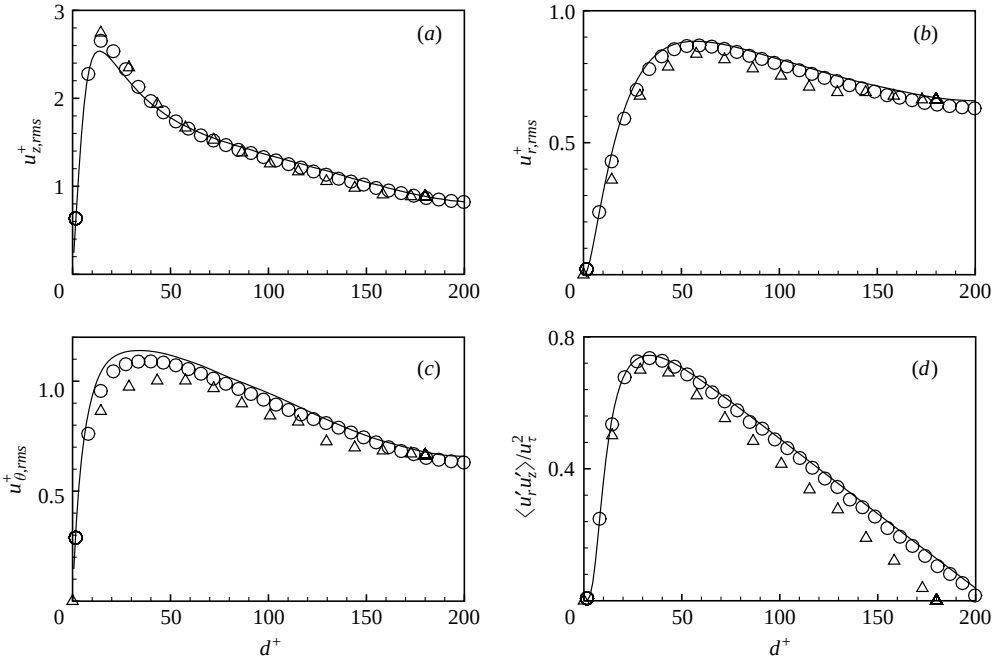

FIGURE 5. Symbols as for figure 3(*b*).

defined by the mean wall shear stress $\overline{\tau}_w$, (2.6). The cross-stream grid refinement tests were performed in order to exclude possible non-physical contamination of the results owing to the employed numerical method. The finest computational mesh includes

Case	EP1	EP2	EP3	EP4	EP5
b/a	0.67	0.67	0.5	0.5	0.5
D_h/a	1.59	1.59	1.30	1.30	1.30
Re_{2a}	7547	7547	9252	9252	9252
Re_{D_h}	6000	6000	6000	6000	6000
$N_x \times N_y$	140×100	200×160	140×100	160×120	200×160
N_z	256	256	256	256	256
a^+	258	256	314	313	312
b^+	173	171	157	157	156
L_z/D_h	6.0	6.0	6.0	6.0	6.0
L_z^+	2472	2453	2450	2443	2431
$h^+_{x,min}$	1.9	1.3	2.3	2.0	1.6
$h^+_{x,max}$	5.4	3.7	6.5	5.7	4.5
$h^+_{y,min}$	1.8	1.1	1.6	1.3	1.0
$h^+_{y,max}$	5.1	3.1	4.6	3.8	2.8
h_z^+	9.7	9.6	9.6	9.5	9.5
Δ^+_{max}	6.4	4.8	6.6	5.9	4.9
Δt^+	0.22	0.37	0.32	0.32	0.16
CFL	0.43	0.69	0.63	0.63	0.32
$T_{av}u_\tau/a$	110	60	100	50	60

TABLE 2. Elliptical duct runs parameters.

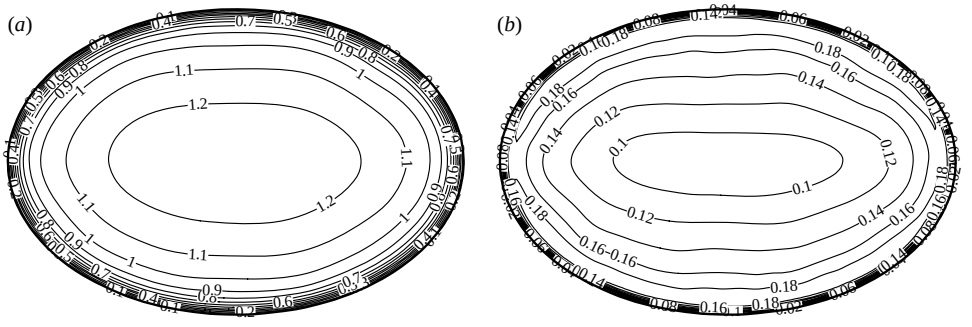

FIGURE 6. Contours of (*a*) U_z, and (*b*) $|\boldsymbol{u}'|_{rms}$, without quadrant averaging (case EP1).

8.192×10^6 grid points, 4.84×10^6 of them inside an elliptical duct for cases EP2 and EP5. The size of the smallest computational cell is about one viscous length unit in the domain cross-section and less than 10 viscous lengths in the streamwise direction. The mean grid width is defined as $\Delta^+ = (h_x^+ h_y^+ h_z^+)^{1/3}$. From table 2, $\Delta^+ \leqslant 5.0$, which means that the constraint $\Delta^+ \leqslant \pi\eta^+$ (see Eggels *et al.* 1994) is satisfied for cases EP2 and EP5. Here, $\eta^+ \approx 1.6$ is the Kolmogorov length scale.

The length of the computational domain $L_z/D_h = 6$ is larger than that in the circular pipe by a factor of 2. Therefore, averaging in time and in the axial direction can be considered adequate, in particular for the simulations with $T_{av}u_\tau/a \geqslant 100$. This is because distributions of mean flow properties become symmetric with respect to the ellipse's principal axes. In figure 6, we show the contours of the averaged axial velocity U_z and the r.m.s. of the velocity total fluctuations $|\boldsymbol{u}'|_{rms}$ (case EP1). It can be seen that the contours are practically symmetrical with respect to the ellipse's axes. Besides the streamwise direction averaging, the reliability of the time-averaged statistics was

Run	EP1	EP2	EP3	EP4	EP5
C_f	0.00932	0.00917	0.00922	0.00917	0.00908
$\Delta(C_f)$	3.6 %	2.1 %	2.6 %	2.1 %	1.0 %
U_c/U_b	1.29	1.29	1.27	1.27	1.28
U_c^+	18.84	19.00	18.72	18.82	18.96
$\max\sqrt{U_x^2+U_y^2}/U_b$	0.0101	0.0104	0.0139	0.0137	0.0135
$\max\|\boldsymbol{u}'\|_{rms}/U_b$	0.198	0.195	0.198	0.197	0.197

TABLE 3. Elliptical duct runs: global characteristics.

increased by additional quadrant averaging over four points located symmetrically to the ellipse's axes. In this paper, all time-averaged statistics are obtained by using averaging over the four quadrants.

Mean flow properties are summarized in table 3. C_f is the friction coefficient computed from the DNS data and $\Delta(C_f)$ is its relative deviation from the correlation based on Blasius' law when it is applied to non-circular ducts by using the hydraulic diameter

$$C_f = 0.0791 Re_{D_h}^{-0.25}, \quad Re_{D_h} = U_m D_h/\nu. \tag{3.1}$$

Comparison of the results shows only minor differences between the friction coefficients C_f obtained for different computational meshes, which indicates that the grid refinement test we performed was successful. In general, our computations confirm the validity of the Blasius' law (3.1) for low-Reynolds numbers considered in this paper. The difference between C_f computed from (3.1) for $Re_{D_h} = 6000$ and that obtained from the Prandtl correlation

$$1/\sqrt{\lambda} = 2\log_{10}(Re_{D_h}\sqrt{\lambda}) - 0.8, \quad C_f = \lambda/4, \tag{3.2}$$

is only 1.2 %.

To calculate the Reynolds number for non-circular ducts, Jones (1976) suggested using a hydraulic diameter D_h', instead of that defined in (2.6), as follows

$$D_h' = D_h \frac{16}{Re_{D_h} C_{flam}}, \tag{3.3}$$

where C_{flam} is the friction coefficient for a fully developed laminar flow in the duct defined in (2.7). For a laminar flow through an elliptical pipe

$$u_z(x, y) = \frac{\Delta p}{2\mu L_z} \frac{a^2 b^2}{a^2 + b^2} \left(1 - \frac{x^2}{a^2} - \frac{y^2}{b^2}\right), \tag{3.4}$$

where μ is a dynamic viscosity. Calculating the bulk velocity U_b from (3.4), for Reynolds number Re'_{D_h}, we have

$$Re'_{D_h} = Re_{D_h} \frac{8a^2 b^2}{D_h^2 (a^2 + b^2)}. \tag{3.5}$$

In our calculations, $Re'_{D_h} = 5844$ and 5680 for $b/a = 0.67$ and 0.5, respectively. Using Re'_{D_h} instead of Re_{D_h} in (3.1) and (3.2) improves the agreement with the friction coefficient obtained by DNS by 0.7 % and 1.4 % for wide and narrow elliptical pipes, respectively.

The global characteristics obtained on different meshes were found to be quite similar. Moreover, the cross-stream section distributions for different meshes were,

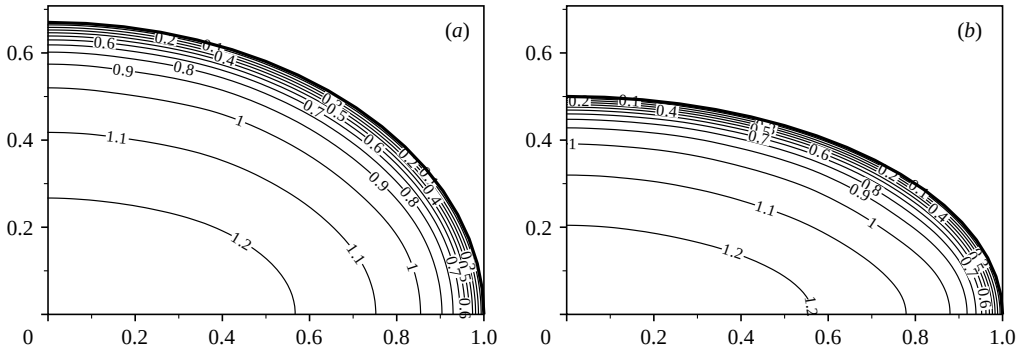

FIGURE 7. Contours of U_z; (*a*)EP2, (*b*)EP5.

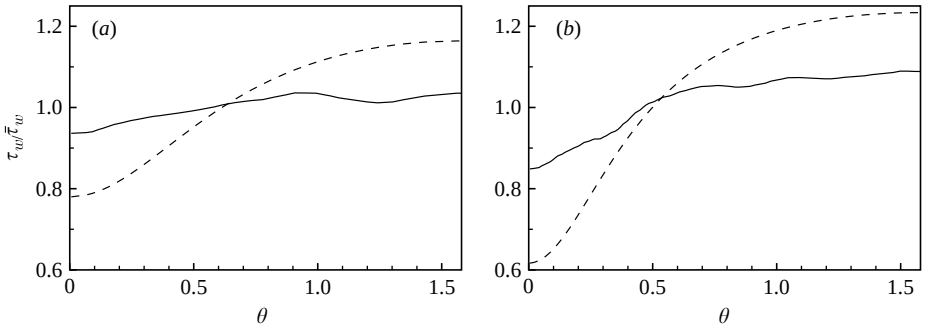

FIGURE 8. Local wall stress; (*a*)EP2, (*b*)EP5. —, turbulent; – – –, laminar.

for the most part, very close quantitatively and qualitatively. For example, the distributions of the axial mean velocity and the turbulence intensities along the major axes were found to be almost identical. This not only confirms the correctness of the results, but is promising evidence that the IB method formulated on Cartesian coordinates can be applied for DNS of the problem at hand. The results presented below were obtained on the finest grids, cases EP2 and EP5 in table 2.

Figure 7 shows the mean streamwise velocity U_z contours for wide and narrow pipes. The corresponding values of U_c/U_b are 1.29 and 1.27. For a laminar profile, (3.4), the velocity contours are a family of ellipses and $U_c/U_b = 2$ for all b/a.

The circumferential variation of the wall shear stress along the wall

$$\tau_w = \mu \left. \frac{\partial U_z}{\partial n} \right|_{wall}, \tag{3.6}$$

normalized by the mean wall shear stress $\overline{\tau}_w$, is shown in figure 8 for the first quadrant $0 \leqslant \theta \leqslant \pi/2$. A certain waviness in the profiles may be attributed to insufficient time averaging or to inaccuracies caused by the velocity interpolation procedure used in the immersed-boundary method. For comparison, the laminar distribution of $\tau_w/\overline{\tau}_w$

$$\frac{\tau_w}{\overline{\tau}_w} = \frac{4ab}{D_h(a^2+b^2)} \left(\frac{a^4 \sin^4\theta + b^4 \cos^4\theta}{a^2 \sin^2\theta + b^2 \cos^2\theta} \right)^{1/2}, \tag{3.7}$$

is also presented in figure 8. The circumferential variation of $\tau_w/\overline{\tau}_w$ for turbulent flow is more moderate than that for laminar flow. The ranges are 0.93–1.04 and 0.85–1.07 for wide and narrow elliptical pipes, respectively; for the laminar flow the

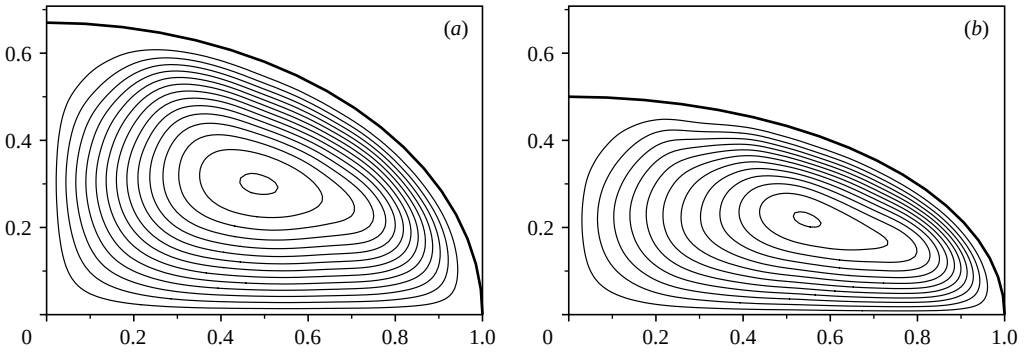

FIGURE 9. Mean secondary flow contours; (*a*)EP2, (*b*)EP5.

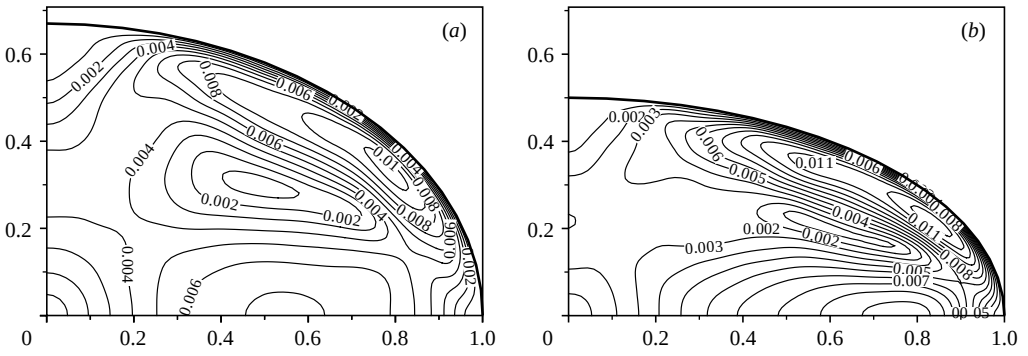

FIGURE 10. Isovels of $U_{xy} = \sqrt{U_x^2 + U_y^2}$; (*a*)EP2, (*b*)EP5.

corresponding ranges are 0.78–1.16 and 0.62–1.23. Similar to laminar flows, the local wall shear stress in turbulent flows is minimal at the points far from the pipe's centre ($x = \pm a$, $y = 0$). The difference between the wall stress τ_w computed at the minor and major axes endpoints is caused by the wall curvature. For a laminar flow, from (3.7), $\tau_w(\theta = 0)/\tau_w(\theta = \pi/2) = b/a$.

The cross-stream mean secondary flow, which develops in non-circular ducts, affects the cross-sectional distribution of the mean streamwise velocity. The cross-flow streamlines of a secondary flow coincide with the contours of the stream function $\psi(x, y)$ defined by $U_x = \partial\psi/\partial y$, $U_y = -\partial\psi/\partial x$ (U_x and U_y are the cross-stream components of the mean velocity vector). Figure 9 shows the streamlines of the secondary flows which appear as two pairs of counter-rotating vortices. (Figure 9 shows a secondary flow in the first quadrant. A similar distribution is seen in the remaining three quadrants.) The secondary vortices transfer low-momentum fluid toward the pipe centre along the minor principal axis of the ellipse. Vice versa, the high-momentum fluid moves towards the wall along the major axis.

The cross-sectional distributions of the secondary-flow velocity $U_{xy} = \sqrt{U_x^2 + U_y^2}$ are shown in figure 10. The maximal values of secondary-flow velocity $\approx 0.010U_b$ and $0.014U_b$ were measured for wide and narrow elliptical pipes, respectively. In our computations, the secondary velocity reaches a maximum value in the vortex periphery, near the wall at $d^+ \approx 15$. For a square duct, Gavrilakis (1992) reported a maximum secondary velocity of $0.019U_b$ found at $d^+ = 10.65$. In the core, the secondary-flow velocity is less. The maximum velocity of the secondary flow along the minor axis U_y

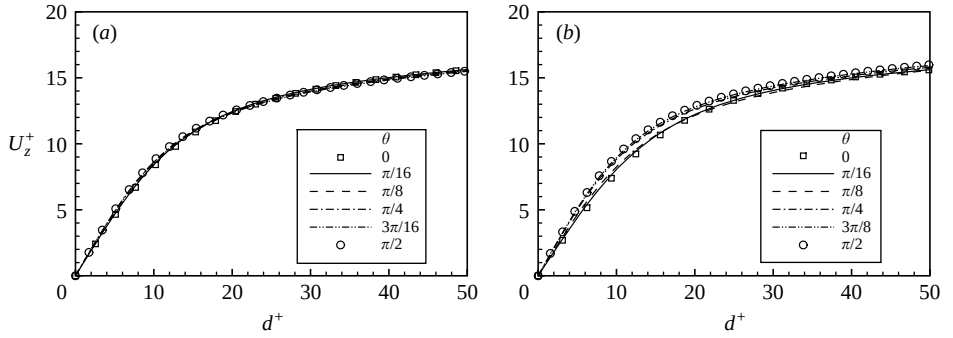

FIGURE 11. Mean streamwise velocity distribution along the lines perpendicular to the wall; (*a*)EP2, (*b*)EP5.

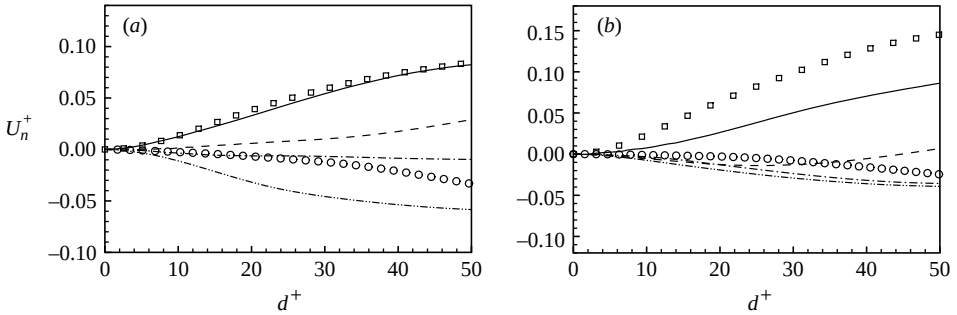

FIGURE 12. Mean secondary flow U_n-velocity distribution along the line perpendicular to the wall; (*a*)EP2, (*b*)EP5. For key see figure 11.

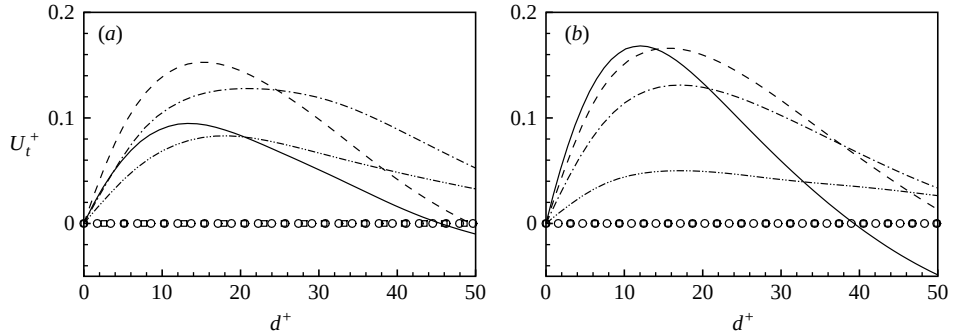

FIGURE 13. Mean secondary flow U_t-velocity distribution along the line perpendicular to the wall; (*a*)EP2, (*b*)EP5. For key see figure 11.

towards the centre is about $0.0045U_b$ for a wide pipe and $0.0035U_b$ for a narrow pipe. The corresponding values for the secondary flow towards the wall along the major axis U_x are $0.0072U_b$ and $0.0105U_b$.

Figures 11–13 show the near-wall profiles of the velocities U_z, U_n and U_t as a function of the distance to the wall d^+, where U_n and U_t are the cross-stream velocity components normal and tangential to the wall, respectively. The location of a (x_w, y_w)-point at the wall is defined by the angle $\theta = \tan^{-1}(y_w/x_w)$.

Figure 11(*a*) shows that the streamwise velocity U_z profile, normalized by the mean shear velocity, is nearly azimuthal symmetric. For a narrow elliptical pipe,

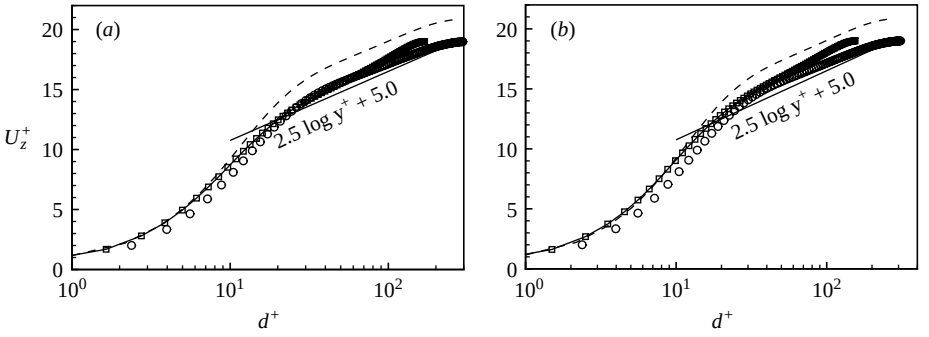

FIGURE 14. Mean streamwise velocity logarithmic profile along the minor (open circles) and major (squares) axes; dashed line – scaling on the local shear velocity.

figure 11(*b*) shows that the velocity distributions along the principal axes are different, but the profiles along the radii with $\theta = \pi/4$ and $3\pi/8$ and that along the minor axis practically coincide. This suggests that the mean streamwise velocity is universal for $\pi/4 \leqslant \theta \leqslant \pi/2$, where the wall curvature is much less than for $0 \leqslant \theta \leqslant \pi/8$. To verify this, in figure 14 the logarithmic plots of the streamwise velocity U_z scaled with the mean shear velocity are shown along the minor and major axes. For a wide elliptical pipe (figure 14*a*), both profiles practically coincide over the interval $20 < d^+ < 100$, indicating very pronounced logarithmic profile. For a narrow pipe, the profiles in figure 14(*b*) show logarithmic regions with different slopes. In addition, the velocity distribution along the major axis exhibits a linear profile $U_z^+ = d^+$ over $0 \leqslant d^+ \leqslant 10$, which is wider than that observed in turbulent pipes and channels. This suggests that possible flow laminarization took place in the vicinity of the major axis endpoints, a point which deserves further comment. Figure 15 shows the Reynolds shear stress $\langle u_n' u_z' \rangle$ distributions scaled with the mean shear velocity u_τ and the correlation coefficient $\langle u_n' u_z' \rangle / (u_{n,rms} u_{z,rms})$. The subscript n stands for the outward-pointing direction normal to the wall. Therefore, $\langle u_n' u_z' \rangle \equiv \langle u_x' u_z' \rangle$ and $\langle u_y' u_z' \rangle$ for $\theta = 0$ and $\pi/2$, respectively. According to figure 15, it can be seen that there is good agreement between the Reynolds shear stress profiles for $\theta = \pi/4$, $3\pi/8$ and $\pi/2$ with those in a circular pipe (figure 5). This means that in the region $\pi/4 < \theta < \pi/2$, the Reynolds stresses are not affected by the wall curvature and therefore the mean wall shear $\overline{\tau}_w$ is a correct scale. On the other hand, the Reynolds shear stress distributions for $\theta = 0$ and $\pi/16$ show strong azimuthal dependency and are considerably less than those calculated in the minor axis vicinity. The argument that this discrepancy is due to unsuitable scaling by $\overline{\tau}_w$ is not supported by the wall shear stress distribution shown in figure 8. Indeed, figure 8 indicates that scaling by the local wall shear stress increases $\langle u_x' u_z' \rangle$ by a factor of 1.08 and 1.18 for wide and narrow elliptical pipes, respectively. Figure 14 presents the streamwise velocity along the major axis normalized by the local shear velocity. Hence, the significant deviation from the universal profile does not support the choice of a local shear velocity as a characteristic velocity.

Figures 16–18 show the turbulent intensities normalized by the wall shear velocity. The plots clearly show the suppression of turbulence along the major axis. For a circular pipe, Eggels *et al.* (1994), discussed the transverse curvature effect as a possible mechanism of turbulence suppression, when the sweep events of carrying high-speed fluid towards the wall followed by the energy transfer to the longitudinal and circumferential components, are inhibited owing to the transverse curvature. For an elliptical pipe, the transverse curvature effect is more significant, leading to

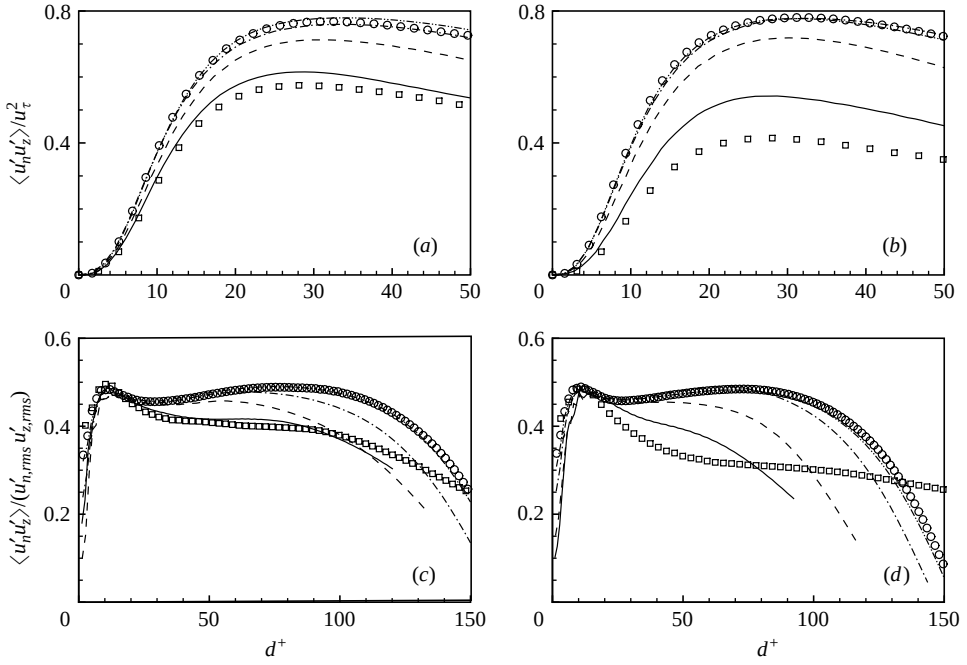

FIGURE 15. The (a, b) Reynolds stress and (c, d) correlation coefficient of u_z' and u_n'; (a, c)EP2, (b, d)EP5. For key see figure 11.

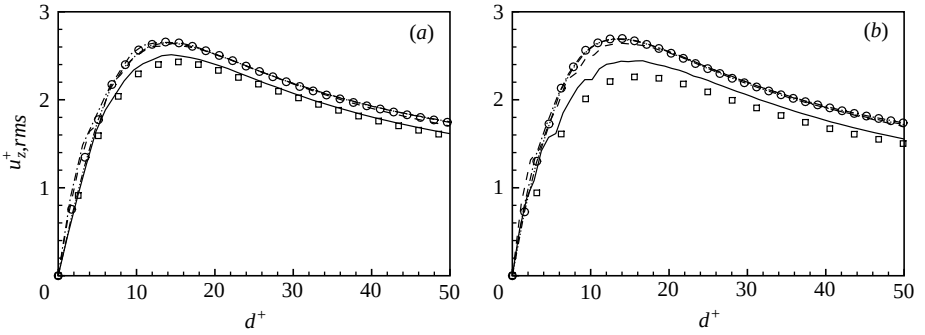

FIGURE 16. Normalized turbulence intensities near the wall, $u_{z,rms}/u_\tau$. For key see figure 11.

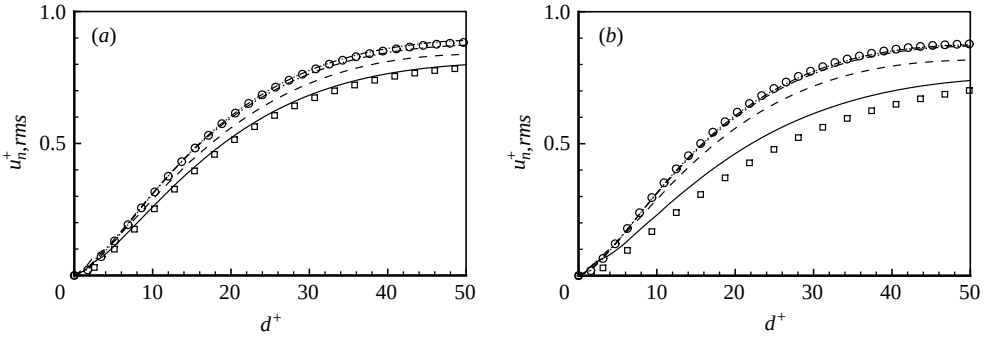

FIGURE 17. Normalized turbulence intensities near the wall, $u_{n,rms}/u_\tau$. For key see figure 11.

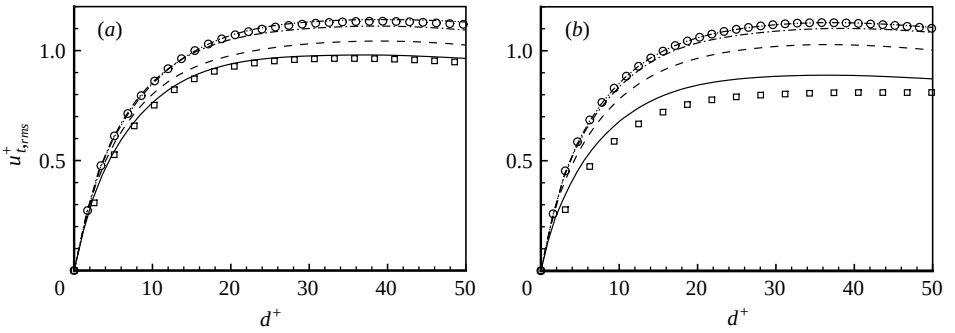

FIGURE 18. Normalized turbulence intensities near the wall, $u_{t,rms}/u_\tau$. For key see figure 11.

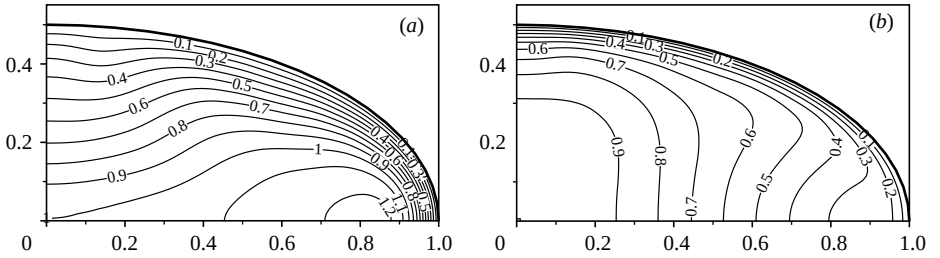

FIGURE 19. U_z-velocity contours. (*a*) 'only-secondary flow', (*b*) 'no-secondary flow'.

considerable reduction of turbulence intensities along a major axis. The distribution of the correlation coefficient $\langle u'_n u'_z \rangle / (u_{n,rms} u_{z,rms})$ along minor and major axes, presented in figures 15(*c*) and (*d*), exhibits considerable differences for $d^+ > 20$.

Notwithstanding that the Reynolds shear stresses $\langle u'_x u'_z \rangle$ measured along the major axis (figure 15) are considerably lower than those observed in pipe and channel turbulent flow, the streamwise velocity profile is in good agreement with the velocity universal logarithmic law (figure 14). To try to understand that, we write the equation for the mean streamwise velocity

$$\overbrace{U_x \frac{\partial U_z}{\partial x} + \frac{\partial \langle u'_x u'_z \rangle}{\partial x}} + \overbrace{U_y \frac{\partial U_z}{\partial y} + \frac{\partial \langle u'_y u'_z \rangle}{\partial y}} = \frac{\Delta p}{\rho L_z} + \nu \left(\frac{\partial^2 U_z}{\partial x^2} + \frac{\partial^2 U_z}{\partial y^2} \right). \tag{3.8}$$

This is the standard Reynolds-averaged Navier–Stokes equation for the streamwise force–momentum balance, where the first and third terms describe the contribution of the cross-stream secondary flow. Each of the four terms of the left-hand side of (3.8) represents a different mechanism of the streamwise momentum fluxes. The cross-stream turbulent and secondary flow momentum transport result in redistribution of the streamwise velocity. To observe the influence of each of these mechanisms, we performed the following numerical experiment. For the given $U_x, U_y, \langle u'_x u'_z \rangle, \langle u'_y u'_z \rangle$ fields, U_z-velocity field was obtained from (3.8) with only the secondary flow transport (i.e. the second and the fourth terms are omitted) or, vice versa, only with the turbulent transport (i.e. the first and the third terms are omitted). In both simulations, the pressure drop Δp in (3.8) corresponds to the turbulent flow with $Re_{D_h} = 6000$. Figure 19 shows the results of this numerical experiment for a narrow pipe, where the streamwise velocity field normalized by the centreline velocity is shown.

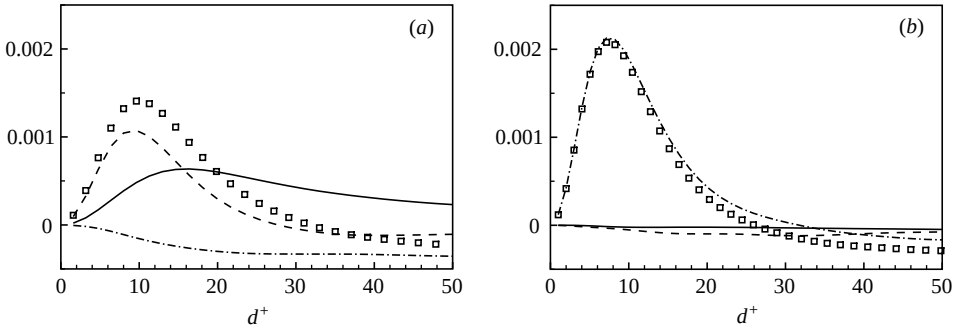

FIGURE 20. Balance of terms in U_z-equation (3.8) along the axes; (a) major axis, $U_y = 0$, —, $U_x \partial U_z/\partial x$, ($b$) minor axis, $U_x = 0$, —, $U_y \partial U_z/\partial y$; ($a$, b): - - -, $\partial\langle u'_x u'_z\rangle/\partial x$; – · –, $\partial\langle u'_y u'_z\rangle/\partial y$; □, all terms.

From figure 19, we can see that these mechanisms play, apparently, opposite roles. In both cases, the resulting velocity field differs considerably from the actual velocity distribution presented in figure 7(b). From figures 7(b) and 19(b), the 'no-secondary flow' field almost does not affect the isovels' patterns in the near-wall region for $\pi/4 \leqslant \theta \leqslant \pi/2$, but changes the flow along the major axis, transferring the low-momentum fluid towards the centre. On the contrary, according to figures 7(b) and 19(a), the 'only-secondary flow' significantly changes the isovels' pattern transferring the high-momentum fluid towards the wall along the major axis and the low-speed fluid towards the centre along the minor axis.

For comparison, figure 20 shows the terms of (3.8) in the near-wall region for a narrow pipe. The momentum transport along the major axis is described by the first two terms in (3.8), where the first term represents the convection of the mean streamwise high-momentum fluid towards the wall. From figure 20(a), the first two terms in (3.8) are of the same order of magnitude, which indicates that the secondary flow along the major axis contributes significantly to the total balance. When we compare the turbulent fluxes of momentum, $\partial\langle u'_x u'_z\rangle/\partial x$ in figure 20(a) to $\partial\langle u'_y u'_z\rangle/\partial y$ in figure 20(b), we can see that the reduced turbulent flux along the major axis is compensated by the induced secondary flow. This might explain why the velocity profile along the major axis replicates the universal logarithmic profile. The third and the fourth terms in (3.8) represent the momentum transport along the minor axis towards the centre. According to figure 20(b), the low-momentum fluid transport along the minor axis by the secondary flow is negligibly small. In the near-wall region $0 \leqslant d^+ \leqslant 10$, the total contribution of the momentum transport along the major axis came out to be much less than that along the minor axis. This reduction results in the linear profile $U_z^+ = d^+$.

The contours of the r.m.s. values of the fluctuating streamwise and cross-sectional velocities, are shown in figures 21 and 22, respectively. Figure 22 clearly demonstrates the azimuthal dependency of the turbulence cross-sectional intensity magnitude. The maximum values are reached relatively close to the minor axis, namely, at $x = 0.2$ and at $x = 0.15$ for wide and narrow elliptical pipes, respectively, at a distance from the wall of $d^+ \approx 40$.

In the near-wall region, the turbulent shear flow is essentially anisotropic. Following Lee, Kim & Moin (1990), we computed the steamwise energy-partition parameter as

$$K^* = \frac{2u_{z,rms}^2}{u_{x,rms}^2 + u_{y,rms}^2}. \tag{3.9}$$

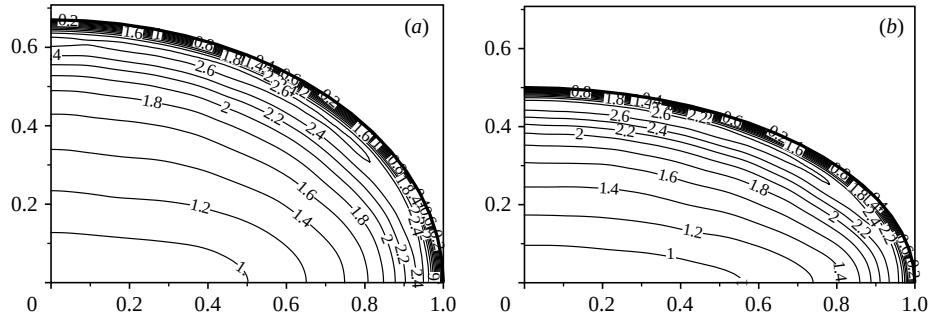

FIGURE 21. Contours of $u_{z,rms}/u_\tau$; (*a*)EP2, (*b*)EP5.

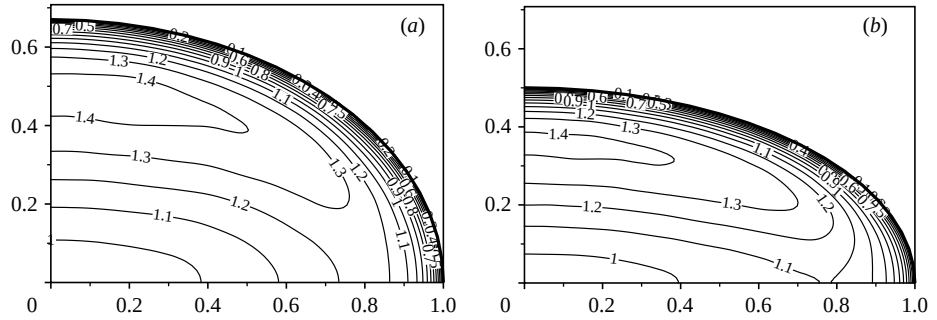

FIGURE 22. Contours of $u_{xy,rms}/u_\tau$, $u_{xy,rms} = \langle u_x'^2 + u_y'^2 \rangle^{1/2}$; (*a*)EP2, (*b*)EP5.

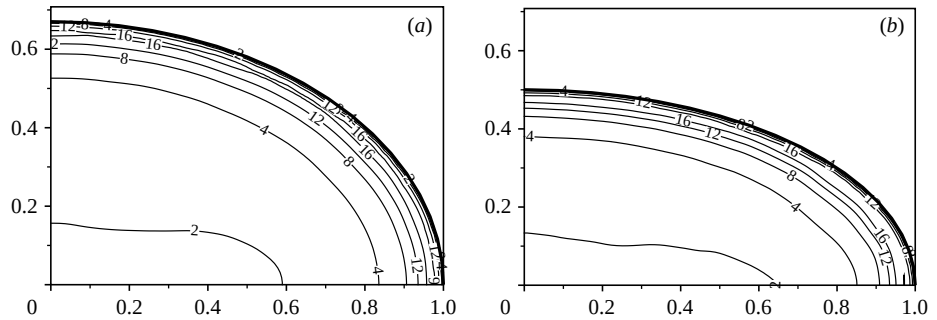

FIGURE 23. Contours of the energy-partition parameter K^*; (*a*)EP2, (*b*)EP5.

In isotropic turbulence $K^* = 1$. In the near-wall regions, a strong shear leads to a much higher value of K^*. Figures 23 and 24 show contours and variations of the energy-partition parameter K^* along the axes. Kim *et al.* (1987) found that for a turbulent channel flow $K^*_{max} \approx 15$ at $d^+ \approx 8$. For a circular pipe, our results obtained in case CP3 are shown in figure 24 for comparison. Following the notation used in this paper, the axes of the major and minor ellipses correspond to $\theta = 0$ and $\theta = \pi/2$, respectively. Profiles of K^* as a function of the distance to the wall d^+ for $0 < \theta < \pi/2$ lie between two (squares and circles) curves and are not shown in figure 24. From figure 24(*a*), it can be observed that the azimuthal dependency of K^* is relatively weak for a wide pipe. For a narrow pipe, the energy-partition parameter in the near-wall region of $0 < d^+ < 7$ is independent of the circumferential location.

The elongated 'streaks' of alternating low- and high-speed fluid generated near the wall are a noteworthy feature of wall-bounded flows. It is commonly held that the

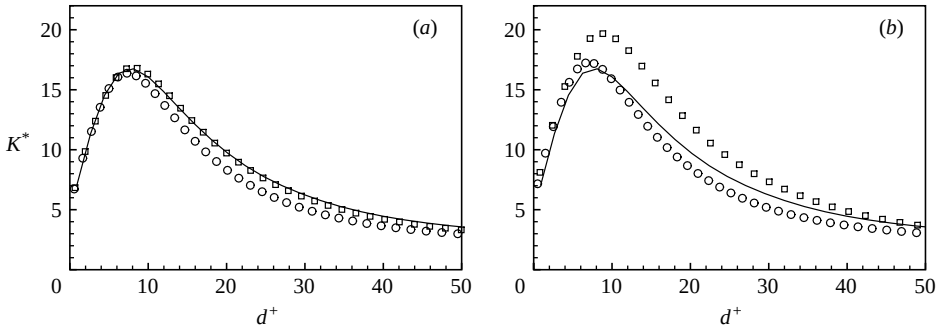

FIGURE 24. Profiles of the energy-partition parameter K^* along ○, the minor and □, major axes; —, circular pipe, case CP3; (*a*)EP2, (*b*)EP5.

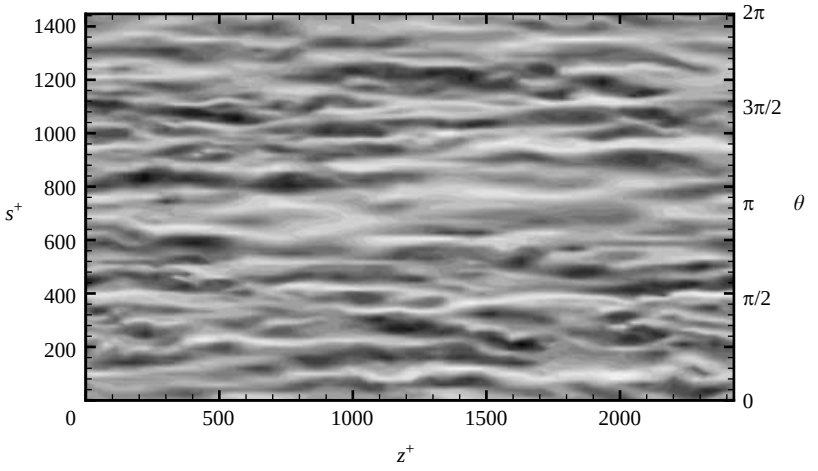

FIGURE 25. Streaks, $d^+ = 10$, EP5.

near-wall streaks have a crucial role in turbulence production. The mean spacing between the streaks in the near-wall region is usually obtained from the two-point autocorrelation function of the streamwise velocity with separations in the spanwise (in our case, azimuthal) direction, $Q_{u'_z u'_z}(\Delta_s)$. It is well-accepted that the half mean streak spacing is the separation Δ_s where the minimum (negative) value of $Q_{u'_z u'_z}$ is reached. The spanwise spacing between the streaks for a channel flow is $\lambda^+ \simeq 80$–120 in wall units for moderate Reynolds number flows.

Contours of the streamwise velocity component at the circumferential surface distanced at $d^+ = 10$ and 50 to the wall are plotted in figures 25 and 26, respectively. Dark and light colours mark high- and low-speed streaks corresponding to $u'_z > 0$ and $u'_z < 0$, respectively. For $d^+ = 50$, the streaks are hardly noticeable (figure 26). In the vicinity of the major axis endpoints (marked by $\theta = 0, \pi, 2\pi$), the streaks are less pronounced, which is indicative of turbulence attenuation by the transverse curvature effect (figure 25). Figure 27 shows the two-point spanwise (azimuthal) autocorrelation function $Q_{u'_z u'_z}(\Delta_s)$ for different d^+. As can be observed, estimating the mean streak spacing yields $\lambda^+ \simeq 100$. The plots presented in figures 24 and 27 are in accordance with the criteria ($K^* > 5$) for the existence of the near-wall streaks for $2 \leqslant d^+ \leqslant 30$–$35$ suggested by Lee *et al.* (1990).

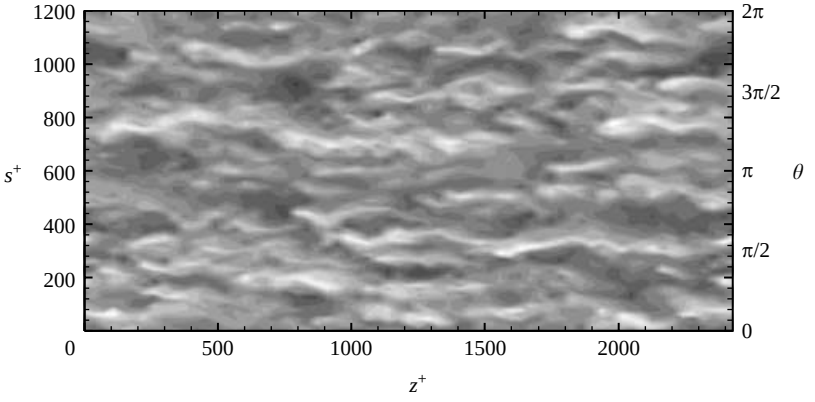

FIGURE 26. Streaks, $d^+ = 50$, EP5.

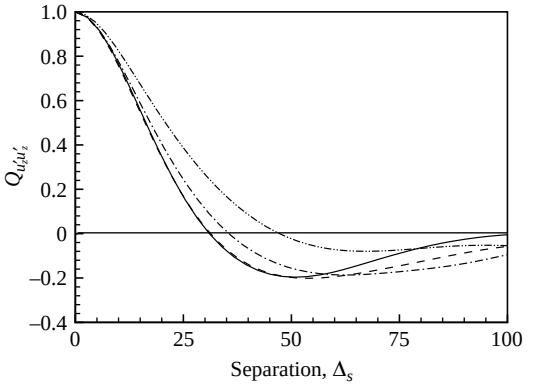

FIGURE 27. Correlation function $Q_{u_z'u_z'}$; —, $d^+ = 10$; – – –, $d^+ = 20$; – · –, $d^+ = 30$; – ·· –, $d^+ = 50$.

4. Summary

Fully developed turbulent flows in non-circular ducts seem relatively simple as they are unidirectional, but they are actually complicated because secondary mean motions develop in the cross-stream plane. These motions are driven by generated mean streamwise vorticity due to the anisotropy of the cross-stream Reynolds stresses. They are an intrinsic feature of turbulent flow in non-circular ducts and play a significant role by cross-stream transferring momentum, heat and mass. An accurate prediction of secondary flows is still difficult for existing turbulent closure models owing to the lack of comprehensive experimental data. Reported DNS-based data on secondary flows have been restricted to the case of a duct with a square cross-section. The aim of the present work was to provide new DNS-based data of turbulent flows in non-circular ducts. We used the immersed-boundary method for Navier–Stokes simulation in complex boundaries. This allows us to simulate flows in ducts with, generally speaking, arbitrary cross-sections by using an efficient and stable calculation procedure derived for simple rectangular meshes. Our results support the recent trend to employ immersed-boundary methods formulated on rectangular meshes as a tool for simulating turbulent flows.

We considered ducts with an elliptic cross-section. Although an elliptical duct is simply a modification of the classic circular pipe, it incorporates the main features of

flows in non-circular ducts. To validate the numerical procedure, DNS of turbulent flows through a circular pipe has been carried out. The results showed good agreement with experimental findings and numerical results reported in the literature. Two elliptical ducts were considered with $b/a = 0.67$ and $b/a = 0.5$ (a and b are the ellipse's principal radii). The Reynolds number was set to $Re_{D_h} = 6000$, based on hydraulic diameter D_h and bulk flow velocity. For both ducts, different meshes were used to exclude possible numerical errors arising from the non-standard computational method employed. The computed friction coefficient was found to be in good agreement with Blasius' law $C_f = 0.0791 Re_{D_h}^{-0.25}$, which supports the validity of the hydraulic diameter concept. The mean streamwise velocity profiles and the turbulence statistics were in good agreement with the known near-wall turbulent characteristics. Cross-stream secondary motions are exhibited by two pairs of vortices which transfer low-momentum fluid towards the duct centre along the minor axis. Vice versa, the high-momentum fluid moves toward the wall along the major axis. The maximum intensity of the secondary flows was found to be 1 % and 1.4 % of bulk velocity for wide and narrow ducts, respectively. Despite this small value, secondary flows play a role comparable with Reynolds stresses for developing the mean velocity profile.

The mean flow characteristics, the Reynolds stresses and turbulence intensities along the minor axis of the elliptical cross-section were found to be similar to plane channel data. The turbulent statistics computed along the major axis is inhibited by the secondary flow transferring high-momentum fluid from the duct's centre towards the wall.

The near-wall distributions of turbulence intensities were studied in detail and showed the significant reduction of turbulent activity in the near-wall region of the major axis endpoints. Moreover, the instantaneous velocity fields in the near-wall region revealed structures similar to the 'streaks', except in the vicinity of the major axis endpoints. This can be attributed to sweep events of carrying high-speed fluid towards the wall, which are inhibited by the wall transverse curvature effect.

This research was supported by The Israel Science Foundation Grant 159/02 and in part by the CAER of The Hebrew University of Jerusalem. The work of N. N. was also supported by The Russian Foundation for Basic Research under Grant 02-01-00492.

REFERENCES

Akselvoll, K. & Moin, P. 1996 An efficient method for temporal integration of the Navier-Stokes equations in confined axisymmetric geometries. *J. Comput. Phys.* **125**, 454–463.

Balaras, E. 2004 Modeling complex boundaries using an external force field on fixed Cartesian grids in large-eddy simulations. *Comput. Fluids* **33**, 375–404.

Cain, D. & Duffy, J. 1971 An experimental investigation of turbulent flow in elliptical ducts. *Intl J. Mech. Sci.* **13**, 451–459.

Choi, H. & Moin, P. 1994 Effects of the computational time step on numerical solutions of turbulent flow. *J. Comput. Phys.* **113**, 1–4.

Demuren, A. O. & Rodi, W. 1984 Calculation of turbulence-driven secondary motion in non-circular ducts. *J. Fluid Mech.* **140**, 189–222.

Eggels, J. G. M., Unger, F., Weiss, M. H., Westerweel, J., Adrian, R. J., Friedrich, R. & Nieuwstadt, F. T. M. 1994 Fully developed turbulent pipe flow: a comparison between direct numerical simulation and experiment. *J. Fluid Mech.* **268**, 175–209.

Fadlun, E. A., Verzicco, R., Orlandi, P. & Mohd-Yusof, J. 2000 Combined immersed-boundary finite-difference methods for three-dimensional complex flow simulations. *J. Comput. Phys.* **161**, 35–66.

Fukagata, K. & Kasagi, N. 2002 Highly energy-conservative finite difference method for the cylindrical coordinate system. *J. Comput. Phys.* **181**, 478–498.

Gavrilakis, S. 1992 Numerical simulation of low-Reynolds-number turbulent flow through a straight square duct. *J. Fluid Mech.* **244**, 101–129.

Harlow, F. H. & Welsh, J. E. 1965 Numerical calculation of time-dependent viscous incompressible flow with free surface. *Phys. Fluids* **8**, 2182–2189.

Huser, A. & Biringen, S. 1993 Direct numerical simulation of turbulent flow in a square duct. *J. Fluid Mech.* **257**, 65–95.

Jiménez. J. & Moin. P. 1991 The minimal flow unit in near-wall turbulence. *J. Fluid Mech.* **225**, 213–240.

Jones, O. C. 1976 An improvement in the calculation of turbulent friction in rectangular ducts. *J. Fluids Engng* **96**, 173–181.

Kim, J., Kim, D. & Choi, H. 2001 An immersed-boundary finite-volume method for simulations of flow in complex geometries. *J. Comput. Phys.* **171**, 132–150.

Kim, J., Moin, P. & Moser, R. 1987 Turbulence statistics in fully developed channel flow at low Reynolds number. *J. Fluid Mech.* **177**, 133–166.

Lee, M., Kim, J. & Moin, P. 1990 Structure of turbulence at high shear rate. *J. Fluid Mech.* **190**, 561–583.

Madabhushi, R. K. & Vanka, S. P. 1993 Direct numerical simulations of turbulent flow in a square duct at low Reynolds number. In *Near-Wall Turbulent Flows* (ed.) R. M. C. So, C. G. Speziale & B. E. Launder, pp. 297–306. Elsevier.

Mohd-Yusof, J. 1997 Combined immersed boundaries/B-splines method for simulations of flows in complex geometries. *CTR Annu. Res. Briefs.* NASA Ames/Stanford University.

Moin, P. 2002 Advances in large eddy simulation methodology for complex flows. *Intl J. Heat Fluid Flow* **23**, 710–720.

Moin, P. & Mahesh, K. 1998 Direct numerical simulation: a tool in turbulence research. *Annu. Rev. Fluid Mech.* **30**, 539–578.

Morinishi, Y., Vasilyev, O. V. & Ogi, T. 2004 Fully conservative finite difference scheme in cylindrical coordinates for incompressible flow simulations. *J. Comput. Phys.* **197**, 686–710.

Moser, R., Kim, J. & Mansour, N. 1999 Direct numerical simulation of turbulent channel flow up to $Re_\tau = 590$. *Phys. Fluids* **11**, 943–945.

Nikitin, N. 1994 Direct numerical modelling of three-dimensional turbulent flows in pipes of circular cross section. *Fluid Dyn.* **29**, 749–757.

Nikitin, N. 1996 Statistical characteristics of wall turbulence. *Fluid Dyn.* **31**, 361–370.

Nikitin, N. 1997 Numerical simulation of turbulent flows in a pipe of square cross section. *Phys. Dokl.* **42**, 158–162.

Peskin, C. S. 1972 Flow patterns around heart valves: a numerical method. *J. Comput. Phys.* **10**, 252–271.

Rai, M. M. & Moin, P. 1991 Direct simulations of turbulent flow using finite-difference schemes. *J. Comput. Phys.* **96**, 15–53.

Schumann, U. 1975 Subgrid scale model for finite difference simulations of turbulent flows in plane channels and annuli. *J. Comput. Phys.* **18**, 376–401.

Spalart, P. R. 1988 Direct simulation of a turbulent boundary layer up to $Re_\theta = 1410$. *J. Fluid Mech.* **187**, 61–98.

Swarztrauber, P. N. 1974 A direct method for the discrete solution of separable elliptic equations. *SIAM J. Numer. Anal.* **11**, 1136–1150.

Verzicco, R. & Orlandi, P. 1996 A finite-difference scheme for three-dimensional incompressible flows in cylindrical coordinates. *J. Comput. Phys.* **123**, 402–414.